J. Fluid Mech. (2000), *vol.* 415, *pp.* 155–174. Printed in the United Kingdom

Modelling low-Reynolds-number effects in the turbulent air flow over water waves

By JAN F. MEIRINK AND VLADIMIR K. MAKIN

Royal Netherlands Meteorological Institute (KNMI), P.O. Box 201, 3730 AE De Bilt, The Netherlands

(Received 14 June 1999 and in revised form 3 March 2000)

In studies of the turbulent air flow over water waves it is usually assumed that the effect of viscosity near the water surface is negligible, i.e. the Reynolds number, $Re = u_*\lambda/\nu$, is considered to be high. However, for short waves or low wind speeds this assumption is not valid. Therefore, a second-order turbulence closure that takes into account viscous effects is used to simulate the air flow. The model shows reasonable agreement with laboratory measurements of wave-induced velocity profiles. Next, the dependence of the dimensionless energy flux from wind to waves, or growth rate, on Re is investigated. The growth rate of waves that are slow compared to the wind is found to increase strongly when Re decreases below 10^4, with a maximum around $Re = 800$. The numerical model predictions are in good agreement with analytical theories and laboratory observations. Results of the study are useful in field conditions for the short waves in the spectrum, which are particularly important for remote sensing applications.

1. Introduction

The air flow over water waves and the consequential growth of the waves are a permanent subject of investigation. The main reason for this is that numerical model predictions of wave growth rates are consistently lower than indicated by measurements (Mastenbroek *et al.* 1996; Belcher & Hunt 1998). Observed growth rates were compiled by Plant (1982) and plotted as a function of c/u_*, where c is the phase velocity of the wave and u_* the friction velocity of the air flow. Considerable scatter is present, which suggests that other parameters may be necessary to explain variations in the growth rate. Such a parameter, which has received little attention so far, is the Reynolds number, $Re = u_*\lambda/\nu$ (here λ is the wavelength and ν the kinematic viscosity of the air). In most studies it is assumed that Re is high enough that dynamic effects of viscosity can be neglected. However, this assumption breaks down for short waves or low wind speeds.

The purpose of the present article is to investigate numerically the influence of the Reynolds number on the structure of the air flow over water waves. This impact is not only important for a proper interpretation of laboratory experiments, but also in the field the assumption that Re is high is sometimes violated, as was concluded in an analysis by Harris, Belcher & Street (1996) of experiments by Snyder *et al.* (1981). Furthermore, Re is especially low for short waves, which are always present on the sea surface. They support a large part of the momentum flux from the atmosphere to the sea (Makin, Kudryavtsev & Mastenbroek 1995) and are important for remote sensing applications.

In numerical simulations of the air flow above waves, the choice of the turbulence closure scheme is crucial. Belcher & Hunt (1993) applied the theory of rapid distortion of turbulence to the description of the flow over hills and waves. From their work, it follows that turbulence closures based on an eddy viscosity concept overestimate stress perturbations in the so-called outer region of the flow. Mastenbroek *et al.* (1996) confirmed this by comparing numerical results from different turbulence models with laboratory observations. They recommended the use of a second-order Reynolds stress closure.

A numerical study taking into account viscous effects was carried out by Harris *et al.* (1996). They used a linear model with an e-ϵ turbulence closure and performed calculations for both coupled and uncoupled air water flow. The eddy viscosity was damped in the outer region to avoid overestimation of the stress perturbations. Simulating the flow over hills they found that the form drag increases considerably when Re drops below 2×10^4.

In this work we solve full nonlinear equations for the air flow and employ a low-Re second-order turbulence closure scheme (Craft & Launder 1996). The numerical model is thought to be general enough to describe the important features of the air flow. In comparison with Harris *et al.* our approach has the advantage that no artificial adjustments to the model have to be made. The model computations are compared with observations performed by Stewart (1970). This experiment is particularly suited for the present investigation, because it was conducted at low Reynolds numbers and covered a wide range of wave ages. Next, growth rates following from the low-Re model are compared with experiments, analytical theories and other numerical models. It is concluded that viscous effects are important when $Re < 10^4$ and lead to enhanced wave growth.

2. Numerical model

The flow of air over a train of monochromatic water waves is investigated. The waves, propagating in the x-direction, give a surface elevation η, which is assumed to be

$$\eta = a\cos(kx - \omega t), \tag{2.1}$$

where a is the amplitude and ω the angular frequency of the wave; k is the wavenumber and t is time. The wind also blows in the x-direction and the water surface is taken to be invariant under translations in the y-direction, so that the remaining problem is two-dimensional. For a wave in deep water the dispersion relation gives

$$\omega^2 = gk + \frac{\gamma}{\rho_w}k^3, \tag{2.2}$$

where g is the acceleration due to gravity, γ the surface tension of water and ρ_w the water density. Finally, the air flow is considered to be statistically steady, incompressible and neutrally stratified.

2.1. *Governing equations and turbulence modelling*

The air flow is governed by the Reynolds-averaged Navier–Stokes equations:

$$\frac{\partial \bar{u}_j}{\partial x_j} = 0, \tag{2.3}$$

$$\frac{\partial \bar{u}_i}{\partial t} + \bar{u}_j \frac{\partial \bar{u}_i}{\partial x_j} = -\frac{1}{\rho}\frac{\partial \bar{p}}{\partial x_i} + \frac{\partial}{\partial x_j}\left(\nu \frac{\partial \bar{u}_i}{\partial x_j} - \overline{u_i' u_j'}\right). \tag{2.4}$$

Here $(u_1, u_2, u_3) \equiv (u, v, w)$ denotes the velocity vector, $(x_1, x_2, x_3) \equiv (x, y, z)$ is the spatial coordinate, p the pressure, ρ the air density and ν the kinematic viscosity of the air. Bars represent Reynolds-averaged quantities and primes denote turbulent fluctuations. In the remainder of this paper the bars above the velocity components and pressure will frequently be dropped for notational convenience.

The above set of equations contains the Reynolds stresses $\overline{u_i' u_j'}$, which must be parameterized. In second-order closure schemes, conservation equations are solved for these turbulent stresses:

$$\frac{\partial \overline{u_i' u_j'}}{\partial t} + \bar{u}_k \frac{\partial \overline{u_i' u_j'}}{\partial x_k} = P_{ij} + d_{ij} + \Pi_{ij} - \epsilon_{ij}, \tag{2.5}$$

where the terms on the right-hand side denote production, diffusion, pressure–velocity correlations and dissipation, respectively. Additionally, an equation is solved for the dissipation rate, ϵ, of turbulent kinetic energy. Most terms in these equations require modelling. In this study, a closure scheme (Craft & Launder 1996) is used which is valid down to the viscous sublayer close to the air–sea interface. This model will be referred to as the low–Reynolds model. It is outlined in detail in the Appendix.

To assess the impact of the Reynolds number, control runs are performed with a second-order model (Launder, Reece & Rodi 1975) that does not take into account viscous effects and is called the high-*Re* model in this paper. Results obtained with this model were presented in Mastenbroek *et al.* (1996). In § 3, it is explained why such advanced closure schemes are used.

2.2. *Computational set-up*

For solution of the conservation equations (2.3), (2.4) and (2.5), the coordinates (x, z) are transformed to wave-following coordinates (χ, ξ): $\chi = k(x - ct)/2\pi$, where $c = \omega/k$ is the wave phase velocity, and $\xi = (z - \eta)/(h - \eta)$, where h is the height of the computational domain.

2.2.1. *Boundary conditions*

The length of the computational domain is one wavelength $\lambda = 2\pi/k$. Periodic conditions are applied at the up- and downstream boundaries. The height of the domain is normally taken as $h = \lambda$. At this height, the wave-induced perturbations are negligible. Therefore, at the upper boundary the horizontal velocity component is specified and the vertical component is set to zero. For the turbulent moments the vertical gradient is set to zero. In boundary layers, the dissipation ϵ is inversely proportional to the distance from the surface. Thus, a proper boundary condition is $\partial(\epsilon z)/\partial z = 0$.

At the lower side of the domain, the orbital velocities of the wave, $u_0 = a\omega \cos(kx - \omega t)$ and $w_0 = a\omega \sin(kx - \omega t)$, are imposed. For the remaining flow variables the numerical treatment of the lower boundary is different in the low-*Re* and the high-*Re* model. In the former, the homogeneous dissipation rate and the Reynolds stresses are set to zero. In the latter, synthetic boundary conditions have to be used, which require specification of the roughness length z_0. Via z_0, the local tangential surface stress along the wave surface is calculated and, subsequently, equilibrium values for the turbulent stresses and the dissipation are imposed. Details on the implementation can be found in Mastenbroek (1996).

2.2.2. *Numerical method and discretization*

The conservation equations listed in § 2.1 comprise a set of ten coupled nonlinear partial differential equations for ten flow variables, subject to the boundary conditions described in § 2.2.1. They are solved in the following way. The momentum equations are rewritten to obtain a Poisson equation for the pressure. This equation is solved using the successive over-relaxation method with Chebyshev acceleration. The conservation equations are then iteratively integrated forward in time with a second-order predictor–corrector method, where, at every timestep, an updated value for the pressure, as obtained by the above method, is used. The difference between integration with a first- and second-order accurate method is used to estimate the optimal size of the next timestep. The calculations start from an initial condition and proceed until a steady state is reached.

For the spatial discretization of the conservation equations, a second-order finite difference method is used. The grid is staggered: the pressure is calculated at cell centres, the other variables at cell edges. To obtain sufficient resolution near the surface, non-uniform meshes are used in which the grid points are closely spaced near the air–water interface and distributed logarithmically away from the surface. Thus, the spacing between two subsequent vertical layers increases with a constant factor. Meshes are chosen such that at least some grid points are within the viscous sublayer, bounded by $z^+ = zu_*/\nu < 5$. A typical mesh has 60 points in the vertical and 32 (uniformly spaced) in the horizontal direction. With these grids, the solution is found to be indifferent to a further increase of the resolution. More detailed information on the numerical implementation can be found in Burgers & Makin (1993).

2.3. *Representation of the data*

In § 4, model results are compared with experimental data. This comparison concerns the vertical profiles of wave-induced perturbations. Let $\tilde{q}$ denote the wave-induced part of a quantity q:

$$\tilde{q} = \bar{q} - \langle \bar{q} \rangle, \tag{2.6}$$

where $\langle\ \rangle$ represents horizontal averaging over a wavelength. In the remainder of this paper, it is also denoted by capitals (e.g. $U = \langle \bar{u} \rangle$). Wave-following coordinates are used in the model, but the averaging can be performed both in Cartesian and in wave-following coordinates.

For the analysis, it is convenient to look at the amplitude $\hat{q}$ of the first harmonic of $\tilde{q}$:

$$\tilde{q} = \tfrac{1}{2}[\hat{q}\mathrm{e}^{2\pi \mathrm{i}\chi} + \hat{q}^*\mathrm{e}^{-2\pi i\chi}] + \text{harmonics}, \tag{2.7}$$

where χ is the wave-following horizontal coordinate and $\hat{q}^*$ denotes the complex conjugate of $\hat{q}$. The complex amplitude is a function of z only. The real part $\mathrm{Re}[\hat{q}]$ gives the amplitude in phase with the wave elevation; the imaginary part $\mathrm{Im}[\hat{q}]$ gives the amplitude in phase with the wave slope. A positive value of $\mathrm{Im}[\hat{q}]$ corresponds to an enhancement of q above the windward slope of the wave.

2.4. *Dimensionless parameters*

At this point it is worthwhile to note which dimensionless parameters determine the solution of the above described problem. The first parameter is the steepness of the wave, ak. When the steepness is low ($ak < 0.1$), the first-order perturbations induced by the wavy surface are of primary importance, and nonlinear effects are small. This means that the growth rate (see § 5) is then independent of ak, which was confirmed,

e.g. by Gent & Taylor's (1976) numerical simulations. In this paper, we will focus on waves with a low steepness.

The ratio of the phase velocity of the wave to the wind speed is the second parameter. It is represented by the wave age, c/u_*. The third parameter is dependent on the model that is used. In the case of the low-Reynolds model, the dynamic effects of viscosity are important. Hence, the actual value of the velocity, which is non-dimensionalized in the Reynolds number, is important. From the various possible definitions of the Reynolds number, we will use $Re = u_*\lambda/\nu$, as was mentioned before. In the high-*Re* model the Reynolds number is assumed to be so large that its actual value does not matter. In exchange, another parameter must be considered: the roughness. Whereas in the low-Reynolds model a smooth surface is assumed, the high-*Re* model captures roughness elements on the surface by employing the dimensionless roughness length kz_0. From the above, it may be clear that the applicability of the low-*Re* model is limited. The computational requirements increase with the range of scales that have to be resolved, from the smallest ν/u_* to the largest λ, and this range grows exactly with the Reynolds number.

3. Characterization of the wave boundary layer

In this section we briefly repeat the framework of the rapid distortion theory of turbulence, as introduced by Belcher & Hunt (1993) for the flow over water waves. Special attention will be paid to the inclusion of viscosity into their scaling arguments.

3.1. *Wave-induced turbulence*

For a proper description of turbulence in the air flow above waves, two timescales are relevant. First, the advection timescale $T_A \sim \lambda/|U(z) - c|$ represents the time it takes for a turbulent eddy to pass over a wave. On this timescale, turbulent eddies feel changes in the velocity gradient of the mean flow. The second timescale T_L (Lagrangian timescale) characterizes the time it takes for an eddy to come into equilibrium with the local velocity gradient. It is the ratio of the typical size, κz, and velocity scale, u_*, of an eddy: $T_L \sim \kappa z/u_*$. Here, $\kappa = 0.41$ is the von Kármán constant.

The wave boundary layer is now divided into an inner and an outer region, where $T_A > T_L$ and $T_A < T_L$, respectively. The location of the top of the inner region, l_H, is given by $T_L \sim T_A$ and it is defined with a proportionality constant such that:

$$kl_H = 2\kappa \frac{u_*}{|U(l_H) - c|}. \tag{3.1}$$

In the inner region close to the water surface, eddies adjust to local conditions before they are substantially transported. On the other hand, in the outer region, they have no time to come into equilibrium with the mean shear; they are rapidly distorted. This implies that the turbulent shear stress perturbations decay quickly in the outer region, because advection smoothes out stress variations over the wave. In § 4 it will be outlined that the shear stress perturbations in the inner region produce asymmetries in the air flow, which finally cause growth of the wave.

This division has consequences for turbulence modelling. In the inner region, where production and dissipation of turbulence are locally in balance, the use of an eddy-viscosity closure is appropriate. However, in the outer region advection of turbulent moments has to be taken into account and this can be done by using a second-order scheme. It was shown by Mastenbroek *et al.* (1996) that, with such a closure, the effects of rapid distortion can be modelled, whereas eddy-viscosity closures fail to

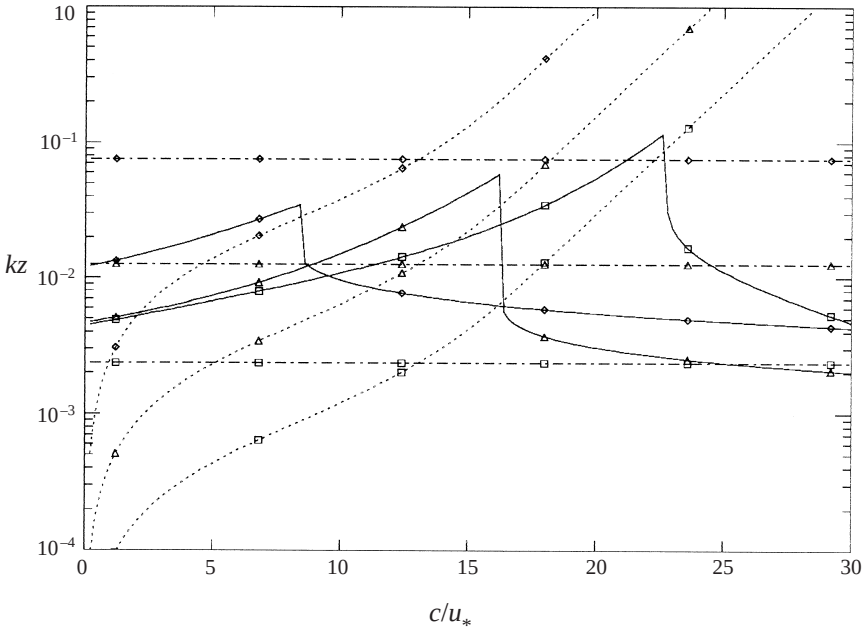

FIGURE 1. Location of layers in the wave boundary layer as a function of wave age: ——, inner region depth kl; — — —, critical height kz_c; — · —, depth of viscous sublayer kz_v. ◇, $Re = 250$; △, $Re = 1500$; □, $Re = 8000$.

reproduce correctly the wave-induced turbulence in the outer region. For this reason, a second-order Reynolds stress model is used in this study.

3.2. *The role of viscosity*

In a viscous layer, perturbations to the shear stress decay on a scale

$$z = \left(\frac{2\nu}{k|U(z) - c|} \right)^{1/2}. \tag{3.2}$$

This fact can be used to generalize (3.1). A rough estimate for the mean horizontal velocity profile is needed. It is obtained by integrating

$$\frac{\partial U}{\partial z} = \frac{u_*^2}{\nu + \nu_t}, \tag{3.3}$$

with the turbulent viscosity ν_t defined as

$$\nu_t(z) = \kappa z u_* f_D(z). \tag{3.4}$$

Here $f_D(z) = 1 - \exp(-z^+/A^+)$, with $A^+ = 28$, is the Von Driest damping function (e.g. Baldwin & Lomax 1978). Now the definition of the inner region depth can be generalized to:

$$kl = \left(\frac{2[\nu + \nu_t(l)]k}{|U(l) - c|} \right)^{1/2}. \tag{3.5}$$

This equation describes the height at which the combination of viscous and turbulent stress perturbations decays.

In figure 1 the inner region depth following from (3.5) is plotted as a function

Case	U_∞ [m s^{-1}]	u_* [m s^{-1}]	Re	c/u_*	U_λ/c	kl	kz_c	kz_v
1	2.27	0.117	3015	6.83	3.46	0.11	0.02	0.06
4	1.02	0.058	1487	13.9	1.58	0.49	0.27	0.13
7	0.56	0.036	867	23.8	0.86	0.03	24	0.22

TABLE 1. Parameters for selected cases of Stewart's experiment.

of the wave age for three different Reynolds numbers. The height of the viscous sublayer, given here by $z_v^+ = 30$, is also shown. For $Re = 8000$, the larger part of the inner region is outside the viscous layer. This means that asymmetry in the flow is mainly created by turbulent stresses. By contrast, when $Re = 250$, the inner region falls completely within the viscous layer and thus molecular forces are responsible for wave growth.

The critical height, z_c, is also plotted. It is the height at which the wind speed equals the phase velocity of the wave: $U(z_c) - c = 0$. For waves that are slow compared to the wind, z_c is low. In contrast, fast waves have a large critical height. It follows from figure 1 that when Re decreases, the range of wave ages for which a wave is considered to be slow, becomes smaller.

4. Comparison with experiment

In this section, model calculations are compared with Stewart's (1970) experiment. In this experiment, detailed observations of the velocity field above water waves were performed. The observations are particularly suited for comparison with the present model, since the Reynolds numbers are low: $Re = 870$–3000. Additionally, the flow can be considered smooth. An indicator for this is the roughness Reynolds number, $Re_r = z_0 u_*/\nu$, which is approximately $Re_r = 0.24$ in Stewart's experiment, whereas an ideally smooth surface would give $Re_r = 0.11$. A wide range of wave ages is covered, which allows a detailed investigation of wave-age dependence. Other laboratory observations of the air flow over water waves include those by Hsu & Hsu (1983) and Mastenbroek *et al.* (1996). However, these are less appropriate for the present purposes, because their Reynolds numbers are fairly high ($6000 < Re < 13\,000$ for Hsu & Hsu and $8700 < Re < 13\,000$ for Mastenbroek *et al.*).

4.1. *Experimental set-up*

Stewart's measurements were carried out in a wind–water tunnel, which was 5.90 m long, 59 cm high and 57 cm wide and contained 21 cm of water. The waves were created by a submerged flat plate, hinged at the bottom. They had a wavelength $\lambda = 40.8$ cm and an amplitude $a = 0.64$ cm (steepness $ak = 0.1$). The waves were short enough not to feel the bottom of the tank, so that the deep-water dispersion relation gives $c = 79.6$ cm s^{-1}. A fan at the downwind end of the tunnel produced a variable wind speed. From the seven reported cases, we pick three to compare with the numerical model. An overview of the free-stream velocities U_∞ for these cases is given in table 1. The instruments were located at 3.96 m from the entrance and 2.74 m from the wave-maker. At this location the boundary-layer depth was about 10 cm. The velocity measurements were performed with hot-wire anemometers.

4.2. *Error estimation*

Stewart gives a detailed estimate of the errors in the observations. The first class of error sources includes the inaccuracy of the electronic measurements, the temperature dependence of the hot wires and the inaccuracy of the calibrations. These lead to an accuracy of the mean velocity within 1.5%. Next, there are geometrical errors in resolving the velocity components, so that part of the horizontal velocity can appear as a vertical velocity. These errors are particularly felt in the wave-induced velocities $\tilde{u}$ and $\tilde{w}$. These quantities are thought to be resolvable to 1% of the mean horizontal velocity. The measurements of the spectra of the wave-induced velocities include contributions from turbulent fluctuations. However, these contributions are found to be small and thus cause little error. The influence of fluctuations in U_∞ on the results was tested by repeating the measurements several times. The magnitude of $\hat{q}$ was found to vary about 20% and the phase about 10°. Finally, the error made in retrieving the data from the plots in Stewart is small enough to be ignored. The error bars in figures 2 to 4 show the largest of the errors above mentioned. However, at the lowest wind speeds, notably in case 7, the accuracy of the hot-wire anemometers is questionable and the error may be larger.

4.3. *Set-up of the simulations*

In the simulations we attempt to approximate the experimental conditions as closely as possible. Special care is necessary for the wind speed. In the model, an open boundary layer is simulated and the flow is driven by U_λ, the mean horizontal wind speed at height $z = \lambda$. In contrast, the experiment is in a tunnel and the flow is forced by a pressure gradient. To define the model runs a value for U_λ is obtained by extrapolating the logarithmic part of the mean horizontal velocity profile of the measurements to the height λ. This leads to the values in table 1.

Of course caution is needed when comparing confined-flow experiments with open-boundary-layer calculations. However, it can be argued (e.g. Yaglom 1979) that the influence of the pressure gradient in a channel flow may be neglected when $z \ll \delta_p$, where δ_p is the pressure gradient lengthscale, which equals the channel half-width. In the experiment $\delta_p = 19\,\text{cm}$ and measurements were taken at $z < 8\,\text{cm}$.

Another parameter to be specified in the high-Re model is the surface roughness z_0. It is obtained from the logarithmic fit through the mean velocity data.

4.4. *Results*

In figures 2 to 4 the observed vertical profiles of the amplitudes of the wave-induced velocity are compared with those computed by the numerical model. The amplitudes are scaled with the wave steepness ak and the velocity at the centre of the channel U_∞. The vertical axis gives the dimensionless height kz above the mean water level.

Figure 2 shows the results for the highest wind speed. This case is typical for a relatively slow wave. The models predict almost the same vertical profiles for the real part of the horizontal, $\text{Re}\,[\hat{u}]$, and the imaginary part of the vertical velocity perturbation, $\text{Im}\,[\hat{w}]$. These two components form the part of the flow in phase with the wave, i.e. in phase with the orbital movement of the water. Compared to the measurements, $\text{Im}\,[\hat{w}]$ is slightly overestimated. The components $\text{Re}\,[\hat{w}]$ and $\text{Im}\,[\hat{u}]$ are created by the work of viscous and turbulent stresses in the inner region. This can be clarified with the out-of-phase part of the momentum conservation equation

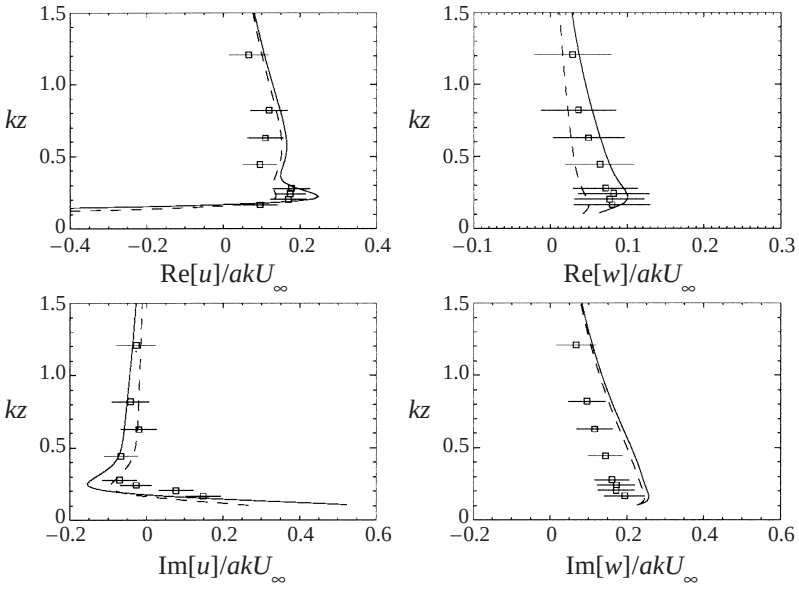

FIGURE 2. Vertical profiles of the wave-induced amplitudes of the horizontal and vertical velocity for case 1: ——, low-*Re* model; — — —, high-*Re* model; □, measurements (Stewart 1970).

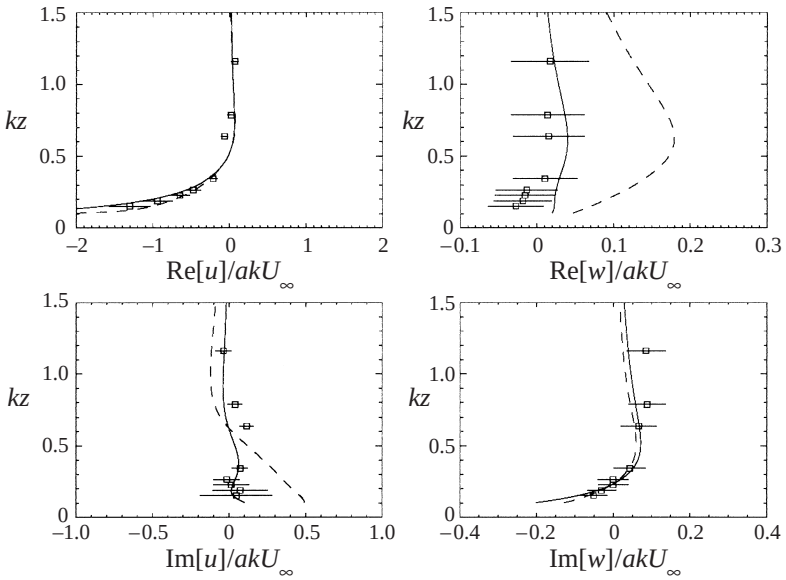

FIGURE 3. As figure 2, but for case 4.

(2.4) for the wave-induced perturbations, which reads in Cartesian coordinates:

$$-(U-c)\,\mathrm{Im}\,[\hat{u}] + \mathrm{Re}\,[\hat{w}]\frac{\mathrm{d}U}{\mathrm{d}kz} = \frac{1}{\rho}\left(\mathrm{Im}\,[\hat{p}] + \frac{\mathrm{d}\,\mathrm{Re}\,[\hat{\tau}]}{\mathrm{d}kz}\right), \tag{4.1}$$

$$(U-c)\,\mathrm{Re}\,[\hat{w}] = \frac{1}{\rho}\left(-\frac{\mathrm{d}\,\mathrm{Im}\,[\hat{p}]}{\mathrm{d}kz} + \mathrm{Re}\,[\hat{\tau}]\right). \tag{4.2}$$

Here, the shear stress τ is the sum of a viscous and a turbulent contribution:

$$\tau = \rho\nu\left(\frac{\partial u}{\partial z} + \frac{\partial w}{\partial x}\right) - \rho\overline{u'w'}. \tag{4.3}$$

Normal turbulent and viscous stresses have been left out for convenience. If there is no stress perturbation acting as a forcing in these equations, then no Re $[\hat{w}]$ and Im $[\hat{u}]$ will be formed. This is the case in inviscid flow. However, a shear stress related to the components Re $[\hat{u}]$ and Im $[\hat{w}]$ produces asymmetry in the flow. The energy flux from the air to the waves can be derived directly, when we note that it is mainly provided by the pressure–slope correlation Im$[\hat{p}]$ at the surface (see § 5.1). This component is found by integrating (4.2) from zero to infinity:

$$\text{Im}\,[\hat{p}]_{z=0} = \int_0^\infty \rho(U-c)\,\text{Re}\,[\hat{w}]\mathrm{d}kz - \int_0^\infty \text{Re}\,[\hat{\tau}]\mathrm{d}kz. \tag{4.4}$$

The component Re $[\hat{w}]$, which is formed in the thin inner region, decays exponentially in the outer region, where it contributes to the slope-correlated pressure according to the first integral on the right-hand side of (4.4). As was noted before, the shear stress perturbations are almost zero in the outer region and thus the contribution of the second integral to the growth rate is normally small. Hence, the magnitude of Re $[\hat{w}]$ gives a good indication of the growth rate. In figure 2 it can be seen that the low-*Re* model predicts a larger Re $[\hat{w}]$ than the high-*Re* model. This corresponds to a higher growth rate at this Reynolds number ($Re \approx 3000$). The measurements are not precise enough to favour one of the two models.

Case 4, which has $Re \approx 1500$ and $c/u_* \approx 14$, is presented in figure 3. The model predictions for the part of the flow in phase with the wave are similar and in agreement with the measurements. The observations further indicate that Re $[\hat{w}]$ is zero, which corresponds to hardly any growth. This is clearly reproduced by the low-*Re* model. However, the high-*Re* model predicts large values for this component. According to this model, a wave with $c/u_* \approx 14$ is in the intermediate regime, i.e. it is in the transition range between slow and fast. For these waves, the highest growth rates are predicted, and thus a large value for Re $[\hat{w}]$ is found. From figure 1 it can be seen that when *Re* becomes lower, the region of intermediate waves shifts to lower wave ages. Therefore, the low-*Re* model treats this wave as a fast wave, meaning no growth and almost zero Re $[\hat{w}]$. Notice that the predicted profile of Im $[\hat{u}]$ also shows good agreement with the measurements.

In figure 4 the wave-induced velocity profiles for case 7 are plotted. This case concerns a fast wave. Here, the wave-induced air flow is practically inviscid. The orbital velocities are dominating, and the part of the flow out of phase with the wave is almost zero. This feature is shown by both models. In this case the way in which stresses are parameterized has hardly any influence on the wave-induced velocity profiles. Therefore, the results from both models are almost the same.

It is unclear why the computations for Im $[\hat{w}]$ differ so much from the observations. The measurements seem to violate continuity. This can be explained by regarding the in-phase part of the continuity equation (in Cartesian coordinates):

$$\text{Re}\,[\hat{u}] = -\frac{\mathrm{d}\,\text{Im}\,[\hat{w}]}{\mathrm{d}kz}. \tag{4.5}$$

While the observations show that the derivative of Im $[\hat{w}]$ tends to zero near the surface, Re $[\hat{u}]$ is large and negative. Possibly, this discrepancy is due to the fact that the wind speed is very low and thus the accuracy of the hot-wire measurements

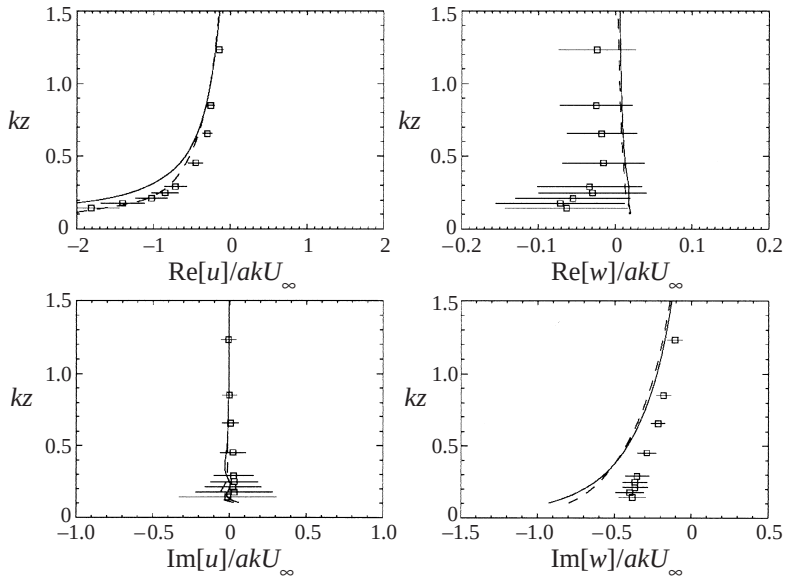

FIGURE 4. As figure 2, but for case 7.

breaks down. The existence of a secondary flow may be a different explanation. Such a secondary flow can arise in the flow over smooth wavy surfaces (Gong, Taylor & Dörnbrack 1996). When it is present, continuity in two dimensions is, of course, not obeyed.

5. Growth rates

In this section some results will be presented concerning the growth rate. This quantity reflects the energy transfer from wind to waves and is crucial as input in wave models. The energy flux, $\dot{E}$, per square metre of water surface from the air to a wave can be written as:

$$\dot{E} = \langle -p(w - \eta_x u) + \tau(u - \eta_x w)\rangle_{\xi=0}, \tag{5.1}$$

with $\eta_x = \partial\eta/\partial x$. A contribution of normal turbulent and viscous stresses to the growth is also present, but it has been omitted here for convenience, as it is small for all wave speeds. For slow waves, the flux is formed mainly by the pressure-slope correlation, while for fast waves the contribution via the shear stress is dominant (see Mastenbroek *et al.* 1996). The energy flux is normally scaled with the energy, E, of the wave per unit surface area. For a sinusoidal wave $E = 0.5\rho_w k c^2 a^2$.

Results will be presented in the form of the growth rate coefficient β, which is defined by

$$\frac{\dot{E}}{\omega E} = \frac{\rho}{\rho_w}\left(\frac{u_*}{c}\right)^2 \beta. \tag{5.2}$$

While (5.1), plus the normal stress contribution, is used to calculate β from the model results, for low steepness it provides insight to linearize (5.1), which leads to:

$$\beta = \frac{(\mathrm{Im}\,[\hat{p}] + \mathrm{Re}\,[\hat{\tau}])_{\xi=0}}{ak\rho u_*^2}. \tag{5.3}$$

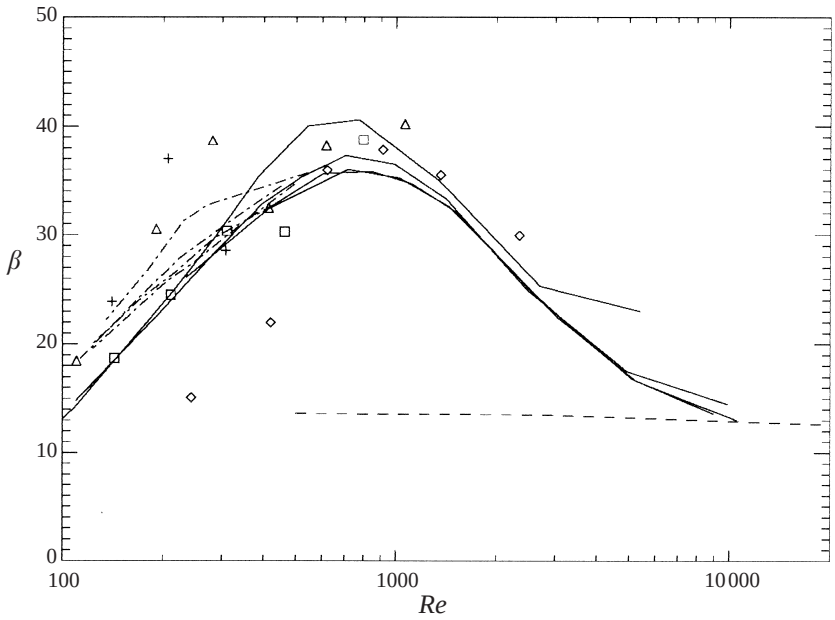

FIGURE 5. Growth rate as a function of Reynolds number. ——, low-*Re* model; — — —, high-*Re* model; — · —, van Gastel *et al.* (1985). Symbols show measurements of Larson & Wright (1975): +, $u_* = 0.12\,\mathrm{m\,s^{-1}}$; □, $u_* = 0.18\,\mathrm{m\,s^{-1}}$; △, $u_* = 0.24\,\mathrm{m\,s^{-1}}$; ◇, $u_* = 0.53\,\mathrm{m\,s^{-1}}$.

5.1. *Impact of Reynolds number on growth rate*

First, attention will be paid to the impact of the Reynolds number on the growth rate of relatively slow waves ($c/u_* < 5$). In figure 5 predictions of the low-*Re* model are compared with measurements by Larson & Wright (1975) and with the analytical model of van Gastel, Janssen & Komen (1985). They presented the growth rates in dimensional form as a function of k for constant u_*. Then, analysis is complicated because the dimensional growth rate increases quadratically with the friction velocity. We present the data in the non-dimensional form of β, as defined in (5.2). The low-*Re*-model results were obtained for low-steepness waves ($ak = 0.01$). The individual curves show results for a constant u_*. Between the curves, u_* varies from 0.14 to $0.9\,\mathrm{m\,s^{-1}}$. The fact that they almost coincide indicates that the Reynolds number is indeed the most important explaining parameter; variations in the wave age cause only slight differences for these slow waves.

Van Gastel *et al.* (1985) described analytically the growth of gravity–capillary waves using linear instability theory. With asymptotic methods, they solved the governing Orr–Sommerfeld equation for the perturbations to a given basic flow, both in the water and in the air. Viscosity was taken into account, but turbulence was neglected. They presented net growth rates; i.e. including dissipation due to the viscosity of the water. To compare with our model, we add to their growth rate results (see their figure 2) the viscous dissipation term $4\nu_w k^2$, where ν_w is the kinematic viscosity of water. The curves, which were obtained for u_* varying between 0.14 and $0.25\,\mathrm{m\,s^{-1}}$, coincide reasonably. The agreement between our model and their analytical results is excellent. This confirms the validity of our numerical model in the very low *Re* range. Although van Gastel *et al.* neglected turbulence, the agreement is perhaps not so surprising, since at these low Reynolds numbers growth is mainly created by viscosity.

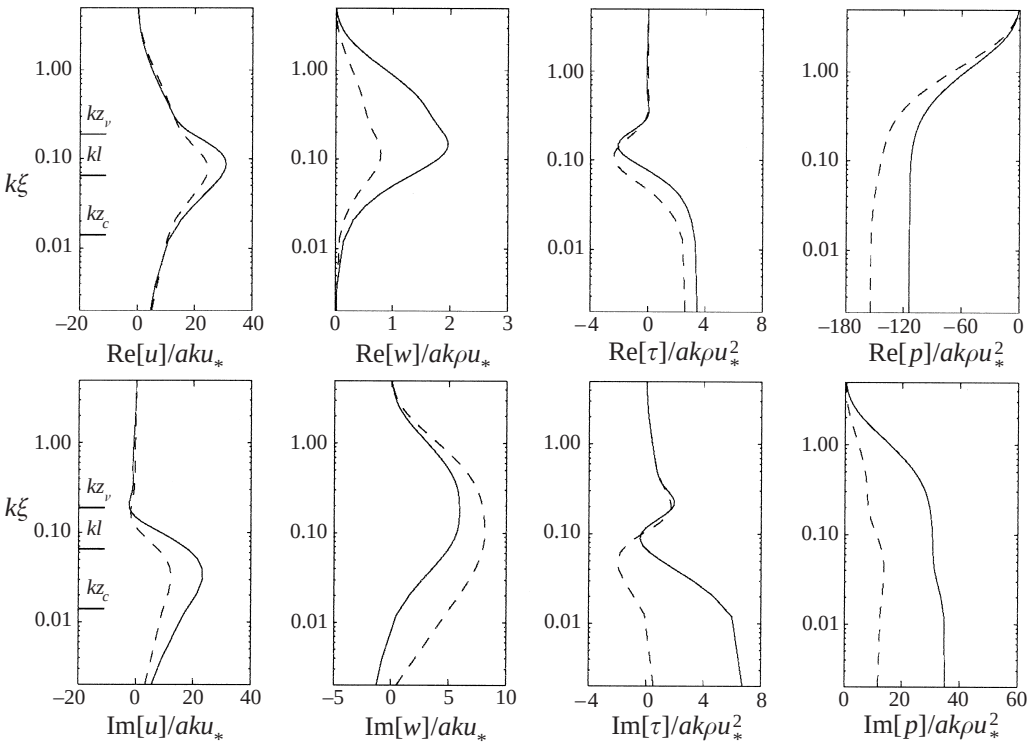

FIGURE 6. Vertical profiles of wave-induced perturbations above a slow wave ($c/u_* = 2$) at $Re = 1000$: ——, low-Re model; — — —, high-Re model. The heights of the critical layer, inner region and viscous sublayer ($z_\nu^+ = 30$) are indicated by horizontal bars.

Larson & Wright (1975) measured growth rates in a laboratory wave tank using microwave backscatter. Their radars were aligned to respond to waves with wavelengths in the range 0.7–7 cm. To isolate the growth due to wind, they added to the measured values the viscous dissipation term, as described above. To non-dimensionalize their growth rates we use values of u_* other than those reported. Donelan & Pierson (1987) pointed out that the reported values are too large, since they were measured at steady state after the wave spectrum had attained its fetch limit. The exponential growth of the waves under consideration, though, took place in the first seconds, when the fetch limit had not yet been reached. Therefore, they proposed alternative values, as listed in the figure caption. Although some scatter in the measurements remains, the general agreement between model and observations is good.

The predicted growth rate shows a maximum $\beta \approx 35$ at $Re \approx 800$. Towards higher Reynolds numbers β decreases and at $Re \approx 10^4$ the difference between low- and high-Re models disappears. Therefore, we conclude that for $Re > 10^4$ the influence of viscosity near the water surface may be neglected. Note that the high-Re model is in principle not dependent on the Reynolds number. However, we used $z_0 = 0.11\nu/u_*$ and thus Re influences the calculations indirectly via the roughness length. From figure 5 it is clear that this influence is small.

The differences between the high- and low-Re models are shown in more detail in figure 6. The figure gives vertical profiles of wave-induced perturbations in wave-following coordinates for $Re = 1000$, which is near the peak of the predicted growth rates. The enhanced growth rate of the low-Re model can be inferred directly from

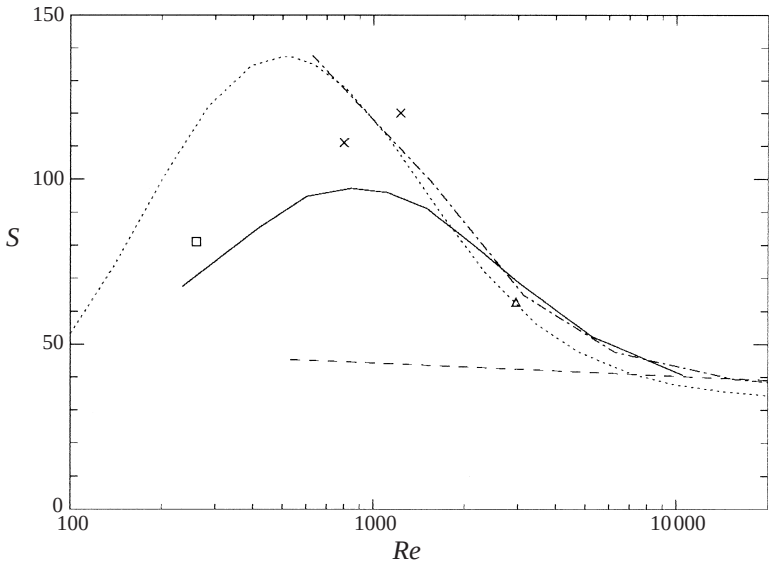

FIGURE 7. Form drag on a smooth hill as a function of Reynolds number: ——, low-*Re* model; — — —, high-*Re* model; — · —, Harris *et al.* (1996); · · ·, Harris (update); △, Zilker & Hanratty (1979); ×, Henn & Sykes (1999); □, Sullivan *et al.* (2000).

the imaginary part of the pressure perturbation. The maximum of $\mathrm{Re}\,[\hat{w}]$ is also clearly much higher in the low-*Re* model. The reason for the increased growth is not completely clear. The maximum around $Re = 800$ is also observed for the form drag of hills (see § 5.2). There we will discuss possible explanations.

5.2. *Form drag on a smooth hill*

We now turn to the limiting case of the flow over smooth stationary rigid waves. In the notation of this article this case is represented by $c = u_0 = w_0 = 0\,\mathrm{m\,s^{-1}}$. The form drag, S, on such hills is the equivalent of the growth rate parameter for waves. It is defined as

$$S = \frac{2\pi\langle p\eta_x\rangle_{\xi=0}}{\rho u_*^2 (ak)^2}. \tag{5.4}$$

Harris *et al.* (1996) found that the form drag on a hill increases strongly when the Reynolds number becomes low, as shown in figure 7. They solved, apart from the base flow, linearized equations for the wave-induced perturbations. Turbulence was modelled by the e-ϵ scheme. This closure is based on an eddy viscosity and thus, as was noted before, overestimates Reynolds-stress perturbations in the outer region. To solve this problem Harris *et al.* damped the eddy viscosity in the outer region. Both the present model and Harris *et al.* show an increase of S for low *Re*. This again gives evidence that viscous effects must be taken into account; the high-*Re* model cannot reproduce the trend of enhanced form drag.

The low-*Re* model predicts a peak of the form drag for $Re \approx 800$; at lower Reynolds numbers S decreases again. For β, in the case of a slowly moving wave, this was also noticed and found in experiments (see § 5.1). In contrast, Harris *et al.* (1996) found no reduction of the form drag towards low Reynolds numbers. However, recent calculations, represented by the dotted line in figure 7, with their model for $Re < 600$ did lead to such a reduction (J. A. Harris, personal communication). The updated

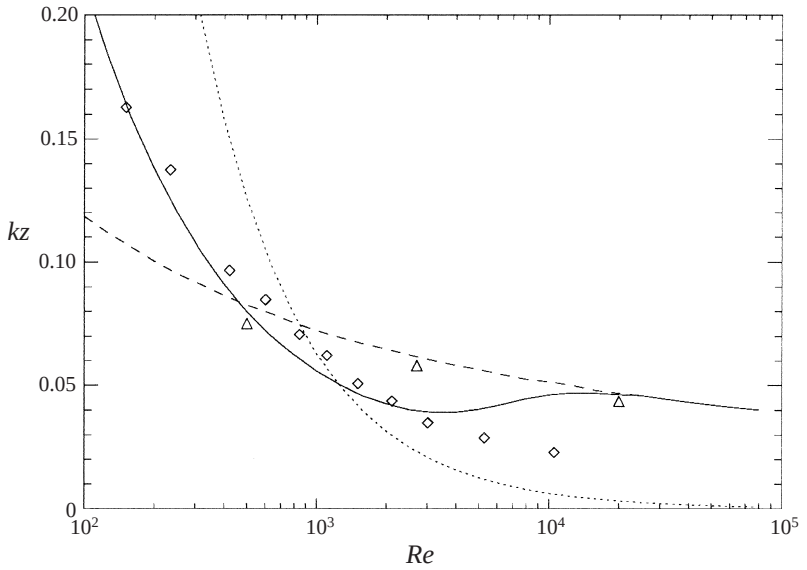

FIGURE 8. Inner region depth in flow over hills: ——, kl from (3.5); — — —, kl_H from (3.1); ···, $z^+ = 10$; symbols denote half the height where max (Re $[\hat{w}]/u_*$) is located, from the low-Re (◇) and high-Re (△) models.

drag values are slightly lower since the definition of their eddy-viscosity damping function was modified to take into account the actual value of the mean velocity profile. Certainly they are considerably higher than predicted by our model, yet a similar trend is found.

In figure 7 the form drag from an experiment by Zilker & Hanratty (1979) is also plotted. It is in good agreement with our low-Re-model predictions. Recently, Henn & Sykes (1999) presented results of their large-eddy simulations of the flow over hills. They found drag values more than twice as large as Zilker & Hanratty. They then claimed that Zilker & Hanratty's form drag was not consistent with an integration of the measured surface pressure data and should therefore be treated with caution. However, Henn & Sykes performed their simulations at a much lower Reynolds number than Zilker & Hanratty. According to the present model results this explains the discrepancy of the form drag values. Sullivan, McWilliams & Moeng (2000) conducted direct numerical simulations of the flow over waves at $Re = 260$. The form drag resulting from their model appears to confirm that S decreases towards very low Reynolds numbers.

An interesting question concerns the existence of a maximum form drag around $Re = 800$. First, we note that a critical layer does not exist over hills, so this can be excluded from our considerations. The depth of the inner region and of the viscous sublayer are expected to be important scales.

The inner region depth is supposed to be related to the height where the maximum of Re $[\hat{w}]$ is located, since Re $[\hat{w}]$ is formed in the inner region and decays exponentially in the outer region, where the shear stress perturbations vanish. Thus, it is useful to compare this height with the estimates for kl, (3.1) and (3.5), given in § 3. These estimates were derived from scaling arguments and are fixed except for an $O(1)$ factor. Hence, they are plotted in figure 8 together with half the height of the maximum of Re $[\hat{w}]$ found in the numerical calculations. A good agreement is found, except at

the highest *Re*. This indicates that the *kl*-estimates are in general consistent with the numerical calculations.

The scale of the viscous sublayer is also plotted. It is defined here at $z^+ = 10$, where the (continued) linear and logarithmic part of the mean velocity profile intersect. Around $Re = 10^3$ the inner region and the viscous sublayer are of comparable depth. For lower *Re* the inner region is located inside the viscous layer. This means that mainly viscous stresses are responsible for creating asymmetry in the flow. In contrast, for higher *Re* the viscous layer is a negligible part of the inner region, so that turbulent stresses cause asymmetry. Around $Re = 10^3$ both mechanisms are active in establishing the form drag. This combination appears to be very effective, leading to a maximum drag.

5.3. *Impact of wave age on growth rate*

So far, we have discussed the flow over hills and slowly moving waves. Now the growth of faster waves is investigated. In figure 9 the growth rate is shown as a function of the wave age. The predictions of the high-*Re* model were presented in Mastenbroek *et al.* (1996). They give rise to the following picture of wave growth (see Belcher & Hunt 1998). Slow waves, with $c/u_* < 10$, have a critical height that is so low that it plays no dynamical role. Growth is caused by the work of stresses in the inner region. With increasing wave age the inner region thickens and the critical layer height increases. Apart from the asymmetry created by turbulent stresses, additional asymmetry could be provided by the critical-layer mechanism (Miles 1957). However, the details of the role of the critical layer in the inner region, which is not inviscid, remain to be clarified. When the wave age increases even further, negative growth from the reverse flow below the critical height becomes important. This explains the sharp drop in β around $c/u_* = 19$. In (4.4) this effect is seen in the $\mathrm{Re}\,[\hat{w}]$ term: below z_c its contribution is negative. Finally, fast waves, with $c/u_* > 20$, have effectively a reverse air flow, which damps the wave. The critical height is so large that it plays no role.

The same picture also seems to be valid for the low-*Re*-model results. There are two differences, however. First, the growth rate curves shift to lower wave ages, when the Reynolds number decreases. This shift must be related to the fact that the critical layer height increases, when *Re* becomes lower (see figure 1). Thus, the definition of slow, intermediate and fast wave regimes, should be altered likewise. Secondly, the magnitude of β for slow waves is higher according to the low-*Re* model, as was already pointed out in § 5.1. This result is in agreement with the parameterization of Plant (1982), who concluded, on the basis of various experimental data, that for slow waves $\beta = 32 \pm 16$.

In figure 9 the growth rate values found in Sullivan *et al.*'s (2000) direct numerical simulations are represented by squares. They are in excellent agreement with our calculations at $Re = 260$, except that, for unclear reasons, we predict a much stronger damping of fast waves.

6. Conclusions

Laboratory observations of the air flow above water waves show that high-*Re* turbulence models cannot correctly reproduce this air flow when its Reynolds number is low. Therefore, corrections are necessary to include effects of viscosity close to the water surface. In this paper a turbulence closure scheme (Craft & Launder 1996) is applied that takes into account such effects.

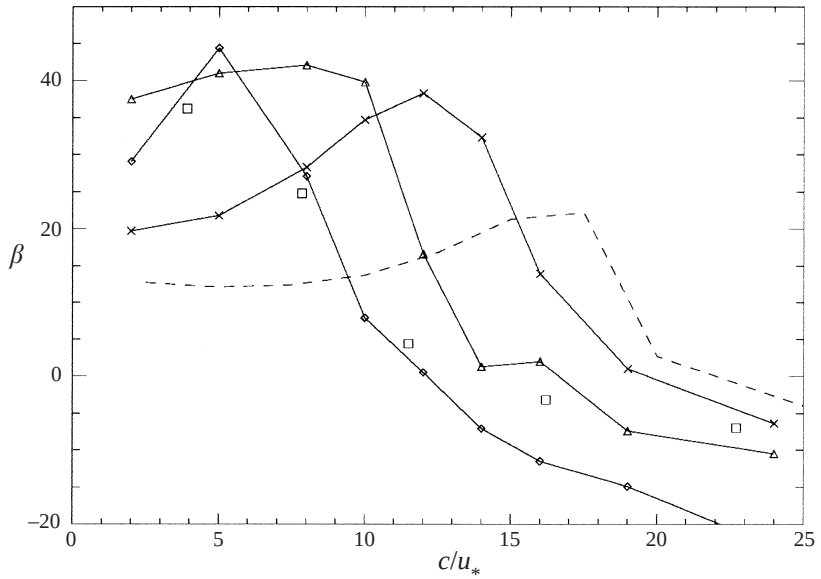

FIGURE 9. Growth rate as a function of wave age: ——, low-*Re* model for ◇, $Re = 260$, △, $Re = 1000$ and ×, $Re = 4000$; — — —, high-*Re* model ($kz_0 = 10^{-4}$); □, direct numerical simulation at $Re = 260$ by Sullivan *et al.* (2000).

In comparison with laboratory observations of the wave-induced velocity field above waves by Stewart (1970) the low-Reynolds model in general leads to improved agreement. In the case with the highest wind speed, the high-*Re* and low-*Re* models perform similarly. In an intermediate case, observations show that the velocity components out of phase with the wave are suppressed. In contrast to the high-*Re* model this is reproduced by the low-*Re* version. Finally, a case with a very low wind speed, and a relatively fast wave, again leads to similar predictions by both models. Here, the wave-induced air flow is practically inviscid, and, thus, the way in which stresses are parameterized is not so important for the velocity perturbation profiles.

A quantity directly following from the velocity, stress and pressure distributions above waves is the growth rate. It is shown that the growth rate of slowly moving waves increases when the Reynolds number becomes smaller than 10^4, with up to a factor 2 for $Re \approx 800$. For smaller Re, the growth rate drops again. A similar maximum is also found for the form drag on smooth stationary waves. It seems to be related to the relative depths of the inner region and the viscous sublayer. These are comparable near the location of the maximum, meaning that viscous and turbulent stresses both play a role in creating growth.

Observed growth rates, e.g. those compiled by Plant (1982), are larger than predicted by advanced turbulence models and exhibit an amount of scatter that is not taken away by a wave age dependence. The present modelling work indicates that the Reynolds number is necessary to explain the growth rates of short laboratory waves. This is confirmed by a comparison with Larson & Wright's (1975) microwave-backscatter experiments. In the field, the enhanced growth also has an impact. If, for example, the wind speed is around $10\,\mathrm{m\,s^{-1}}$, corresponding to $u_* \approx 0.4\,\mathrm{m\,s^{-1}}$, then viscous effects will be important for the waves in the spectrum with $\lambda < 40\,\mathrm{cm}$. The waves in this range support most of the momentum flux from the atmosphere to the sea and are important for remote sensing applications.

It is a pleasure to thank Vladimir Kudryavtsev for fruitful discussions. We also thank Professor Battjes for his interest in this work. J. F. M. was financially supported by the Netherlands Organisation for Scientific Research (NWO), Division Earth and Life Sciences (ALW). V. M. acknowledges the Office of Naval Research (ONR grant N00014-98-1-0437, PR 98PR04572-00) and the International Association (reference INTAS 96-1817 and INTAS/CNES 97-0222). Finally, we are grateful for the many useful comments made by the referees.

Appendix. Description of the low-Reynolds-number model

The formulation of the second-order turbulence closure for low Reynolds numbers applied in this work follows Craft & Launder (1996). Modifications include the neglect of terms that are not important for the flow we consider. A special feature of the closure is that no wall-normal vectors are used. To still be able to identify near-surface effects, the flatness parameter, A, is introduced. It is defined as

$$A = 1 - \tfrac{9}{8}(A_2 - A_3), \tag{A 1}$$

where $A_2 = a_{ij}a_{ij}$ and $A_3 = a_{ij}a_{jk}a_{ki}$ are the second and third invariants of the dimensionless stress anisotropy, a_{ij}, respectively:

$$a_{ij} = \frac{\overline{u_i'u_j'}}{e} - \tfrac{2}{3}\delta_{ij}, \tag{A 2}$$

where $e = \frac{1}{2}\overline{u_i'u_i'}$ is the turbulent kinetic energy. The flatness parameter is one in isotropic turbulence and vanishes near a surface, where the turbulent fluctuations reduce to a two-component form.

The closure of the terms in (2.5) for the Reynolds stresses is as follows.

The production term needs no parameterization:

$$P_{ij} = -\left(\overline{u_i'u_k'}\frac{\partial \bar{u}_j}{\partial x_k} + \overline{u_j'u_k'}\frac{\partial \bar{u}_i}{\partial x_k}\right). \tag{A 3}$$

The diffusion term reads

$$d_{ij} = \frac{\partial}{\partial x_k}\left(\nu\frac{\partial \overline{u_i'u_j'}}{\partial x_k} - \overline{u_i'u_j'u_k'}\right). \tag{A 4}$$

The triple correlation appearing in this expression is modelled as

$$\overline{u_i'u_j'u_k'} = -c_s\frac{e}{\epsilon}\left(\overline{u_i'u_l'}\frac{\partial \overline{u_j'u_k'}}{\partial x_l} + \overline{u_j'u_l'}\frac{\partial \overline{u_k'u_i'}}{\partial x_l} + \overline{u_k'u_l'}\frac{\partial \overline{u_i'u_j'}}{\partial x_l}\right), \tag{A 5}$$

with $c_s = 0.11$.

The pressure correlation term is modelled as in Craft, Ince & Launder (1996). It is split into two parts: $\Pi_{ij} = \phi_{ij} + d_{ij}^p$. Here, the pressure–diffusion term, d_{ij}^p, is incorporated in d_{ij}. The pressure–strain correlation, ϕ_{ij}, reads

$$\phi_{ij} = \overline{\frac{p'}{\rho}\left(\frac{\partial u_i'}{\partial x_j} + \frac{\partial u_j'}{\partial x_i}\right)}. \tag{A 6}$$

For modelling it is split into:

$$\phi_{ij1} = -c_1\tilde{\epsilon}\left[a_{ij} + c_1'\left(a_{ik}a_{kj} - \tfrac{1}{3}A_2\delta_{ij}\right)\right] - \tilde{\epsilon}Aa_{ij} \tag{A 7}$$

$$\phi_{ij2} = -0.6\left(P_{ij} - \tfrac{1}{3}\delta_{ij}P_{kk}\right) + 0.3a_{ij}P_{kk}$$
$$-\frac{0.2}{e}\left[\overline{u_k'u_j'}\,\overline{u_l'u_i'}\left(\frac{\partial \bar{u}_k}{\partial x_l} + \frac{\partial \bar{u}_l}{\partial x_k}\right) - \overline{u_l'u_k'}\left(\overline{u_i'u_k'}\frac{\partial \bar{u}_j}{\partial x_l} + \overline{u_j'u_k'}\frac{\partial \bar{u}_i}{\partial x_l}\right)\right] \qquad (A\,8)$$
$$-c_2[A_2(P_{ij} - D_{ij}) + 3a_{mi}a_{nj}(P_{mn} - D_{mn})].$$

Here,

$$D_{ij} = -\left(\overline{u_i'u_k'}\frac{\partial \bar{u}_k}{\partial x_j} + \overline{u_j'u_k'}\frac{\partial \bar{u}_k}{\partial x_i}\right) \qquad (A\,9)$$

and the coefficients are

$$c_1 = (3.75A_2^{1/2} + 1)A, \qquad c_1' = 0.7, \qquad c_2 = 0.6.$$

The homogeneous dissipation rate $\tilde{\epsilon}$, appearing in (A 7), is related to the kinematic dissipation rate ϵ by

$$\tilde{\epsilon} = \epsilon - 2\nu\left(\frac{\partial e^{1/2}}{\partial x_j}\right)^2. \qquad (A\,10)$$

The stress dissipation, finally, is taken to be:

$$\epsilon_{ij} = f_\epsilon 2\epsilon\frac{\epsilon_{ij}'}{\epsilon_{kk}'} + (1 - f_\epsilon)\tfrac{2}{3}\epsilon\delta_{ij}, \qquad (A\,11)$$

where

$$\epsilon_{ij}' = \epsilon\frac{\overline{u_i'u_j'}}{e} + 2\nu\left(\frac{\overline{u_l'u_n'}}{e}\frac{\partial e^{1/2}}{\partial x_l}\frac{\partial e^{1/2}}{\partial x_n}\delta_{ij} + \frac{\overline{u_l'u_i'}}{e}\frac{\partial e^{1/2}}{\partial x_j}\frac{\partial e^{1/2}}{\partial x_l} + \frac{\overline{u_i'u_j'}}{e}\frac{\partial e^{1/2}}{\partial x_i}\frac{\partial e^{1/2}}{\partial x_l}\right). \qquad (A\,12)$$

The coefficient f_ϵ manages the transition from isotropic dissipation in the fully turbulent part of the flow to anisotropic dissipation towards the surface. Following Launder & Li (1994) we take

$$f_\epsilon = \exp(-20A^2). \qquad (A\,13)$$

To close the system, the following conservation equation for the homogeneous dissipation rate is solved:

$$\frac{\partial \tilde{\epsilon}}{\partial t} + \bar{u}_k\frac{\partial \tilde{\epsilon}}{\partial x_k} = c_{\epsilon 1}\frac{\tilde{\epsilon}P_{kk}}{2e} - c_{\epsilon 2}\frac{\tilde{\epsilon}^2}{e} - c_{\epsilon 2}'\frac{(\epsilon - \tilde{\epsilon})\tilde{\epsilon}}{e}$$
$$+\frac{\partial}{\partial x_l}\left[\left(\nu\delta_{lk} + c_\epsilon\overline{u_l'u_k'}\frac{e}{\epsilon}\right)\frac{\partial \tilde{\epsilon}}{\partial x_k}\right] + c_{\epsilon 3}\nu\overline{u_i'u_j'}\frac{e}{\epsilon}\frac{\partial^2 \bar{u}_k}{\partial x_i \partial x_l}\frac{\partial^2 \bar{u}_k}{\partial x_j \partial x_l}, \qquad (A\,14)$$

where the coefficients are

$$c_{\epsilon 1} = 1.0, \qquad c_{\epsilon 2}' = 1.0, \qquad c_{\epsilon 3} = 1.75, \qquad c_\epsilon = 0.18,$$

$$c_{\epsilon 2} = \frac{1.92}{1 + 0.7A_dA_2^{1/2}}, \qquad A_d = \max(0.2, A).$$

The constant $c_{\epsilon 3}$ was used to tune the model such that it reproduces the law of the wall for a flat plate boundary layer. Its value is somewhat higher than mentioned in Craft & Launder (1996), which can be explained by the omission of their $c_{\epsilon 4}$ term.

REFERENCES

Baldwin, B. & Lomax, H. 1978 Thin layer approximation and algebraic model for separated turbulent flow. *AIAA Paper*, 78–257.

Belcher, S. E. & Hunt, J. C. R. 1993 Turbulent shear flow over slowly moving waves. *J. Fluid Mech.* **251**, 109–148.

Belcher, S. E. & Hunt, J. C. R. 1998 Turbulent flow over hills and waves. *Ann. Rev. Fluid Mech.* **30**, 507–538.

Burgers, G. & Makin, V. K. 1993 Boundary layer model results for wind–sea growth. *J. Phys. Oceanogr.* **23**, 372–385.

Craft, T. J., Ince, N. Z. & Launder, B. E. 1996 Recent developments in second-moment closure for buoyancy-affected flows. *Dyn. Atmos. Oceans* **23**, 99–114.

Craft, T. J. & Launder, B. E. 1996 A Reynolds stress closure designed for complex geometries. *Intl J. Heat and Fluid Flow* **17**, 245–254.

Donelan, M. A. & Pierson, W. J. 1987 Radar scatter and equilibrium ranges in wind-generated waves with applications to scatterometry. *J. Geophys. Res.* **92**, 4971–5029.

Gastel, K. van, Janssen, P. A. E. M. & Komen, G. J. 1985 On phase velocity and growth rate of wind-induced gravity–capillary waves. *J. Fluid Mech.* **161**, 199–216.

Gent, P. R. & Taylor, P. A. 1976 A numerical model of the air flow above water waves. *J. Fluid Mech.* **77**, 105–128.

Gong, W., Taylor, P. A. & Dörnbrack, A. 1996 Turbulent boundary-layer flow over fixed aerodynamically rough two-dimensional sinusoidal waves. *J. Fluid Mech.* **312**, 1–37.

Harris, J. A., Belcher, S. E. & Street, R. L. 1996 Linear dynamics of wind-waves in coupled turbulent air–water flow. Part 2. Numerical model. *J. Fluid Mech.* **308**, 219–254.

Henn, D. S. & Sykes, R. I. 1999 Large-eddy simulation of flow over wavy surfaces. *J. Fluid Mech.* **383**, 75–112.

Hsu, C.-T. & Hsu, E. Y. 1983 On the structure of turbulent flow over a progressive water wave: theory and experiment in a transformed, wave-following coordinate system. Part 2. *J. Fluid Mech.* **131**, 123–153.

Larson, T. R. & Wright, J. W. 1975 Wind-generated gravity–capillary waves: laboratory measurements of temporal growth rates using microwave backscatter. *J. Fluid Mech.* **70**, 417–436.

Launder, B. E. & Li, S.-P. 1994 On the elimination of wall-topography parameters from second-moment closure. *Phys. Fluids* **6**(2), 999–1006.

Launder, B. E., Reece, G. J. & Rodi, W. 1975 Progress in the development of a Reynolds-stress turbulence closure. *J. Fluid Mech.* **68**, 537–566.

Makin, V. K., Kudryavtsev, V. N. & Mastenbroek, C. 1995 Drag of the sea surface. *Boundary-Layer Met.* **73**, 159–182.

Mastenbroek, C. 1996 Wind–wave interaction. PhD thesis, Delft Technical University.

Mastenbroek, C., Makin, V. K., Garat, M. H. & Giovanangeli, J. P. 1996 Experimental evidence of the rapid distortion of turbulence in the air flow over water waves *J. Fluid Mech.* **318**, 273–302.

Miles, J. W. 1957 On the generation of surface waves by shear flow. *J. Fluid Mech.* **3**, 185–204.

Plant, W. J. 1982 A relation between wind stress and wave slope. *J. Geophys. Res.* **87**(C3), 1961–1967.

Snyder, R. L., Dobson, F. W., Elliott, J. A. & Long, R. B. 1981 Array measurements of atmospheric pressure fluctuations above surface gravity waves. *J. Fluid Mech.* **102**, 1–59.

Stewart, R. H. 1970 Laboratory studies of the velocity field over deep-water waves. *J. Fluid Mech.* **42**, 733–754.

Sullivan, P. P., McWilliams, J. C. & Moeng, C.-H. 2000 Simulation of turbulent flow over idealized water waves. *J. Fluid Mech.* **404**, 47–85.

Yaglom, A. M. 1979 Similarity laws for constant-pressure and pressure-gradient turbulent wall flows. *Ann. Rev. Fluid Mech.* **11**, 505–540.

Zilker, D. P. & Hanratty, T. J. 1979 Influence of the amplitude of a solid wavy wall on a turbulent flow. Part 2. Separated flows. *J. Fluid Mech.* **90**, 257–271.